Carbonation curing of mortars produced with reactivated cementitious materials for CO_2 sequestration

Ye Li[a], Dongsheng Han[a], Haodong Wang[a], Hanxiong Lyu[a, b], Dujian Zou[a], Tiejun liu[a, *]

[a] School of Civil and Environmental Engineering, Harbin Institute of Technology, Shenzhen, PR China

[b] Department of Civil and Environmental Engineering, Hong Kong Polytechnic University, Hong Kong

* Corresponding author. Tel.: +86-0755-26033368

Email adresses : liye@hit.edu.cn (Ye Li), 20S054030@stu.hit.edu.cn (Dongsheng Han), 15818602282@163.com (Haodong Wang), hitmselhx@163.com (Hanxiong lyu), zoudujian@163.com (Dujian Zou), liutiejun@hit.edu.cn (Tiejun Liu)

Abstract

Low-carbon emission mortar samples were prepared using reactivated cementitious materials (RCMs) produced by calcinating hydrated cement paste with adjusted Ca/Si ratios. Carbonation curing was employed to enhance the cementing capacity of the RCMs and to sequestrate CO2. The compressive strength, phase assemblage, microstructure, and environmental impacts of the mortars were analyzed. According to the results, the mortar sample produced with the RCM with a 10% addition of silica fume during calcination attained the highest compressive strength (35.3 MPa) after water curing, while higher silica contents were unfavorable because the low-lime calcium silicates that formed have limited water reactivity. Carbonation curing significantly promoted reactions of the RCMs and, thus, the compressive strength of the mortars compared to water curing. The amorphous and metastable calcium carbonates contributed more to the densification of the microstructure than the calcite. From the life cycle assessment, the RCM mortars had a significantly lower impact on global warming potential compared to Portland cement mortars.

Keywords: reactivated cementitious material, waste cement paste, carbonation, CO_2 sequestration

1. Introduction

Over the last few decades, the construction industry has encountered a range of significant challenges due to its excessive consumption of natural resources, substantial contribution to the greenhouse gas emission, and the creation of construction and demolition waste (CDW). Approximately 4.4 billion tons of cement–an essential ingredient in the production of concrete and mortar–were produced worldwide in 2021 (Summaries, 2021). The cumulative CO_2 emissions associated with the manufacturing of cement from 1928 to 2018 reached 38.3±2.4 Gt (Andrew, 2019), which represents about 5–8% of global CO_2 emissions from all industrial processes (Barcelo et al., 2013; Pade and Guimaraes, 2007). Thus, a drastic reduction in CO_2 emissions from cement production is critical in order to meet the reduction in carbon release required to limit the global temperature rise to 2 °C (Churkina et al., 2020; Müller et al., 2013). At the same time, the continuing increase in the world population means that the demand for cement will nevertheless continue to rise for the benefit of mankind's well-being.

Nearly 60% of total emissions during cement production originates from the calcination and decarbonation processes of limestone (Andrew, 2019), the remainder arising from the consumption of energy and fossil fuels during the clinkering process at temperatures exceeding 1,450 °C. Therefore, any options to reduce the CO_2 footprint of cement must imperatively involve producing economically and environmentally viable cement alternatives utilizing low calcium raw materials, lower clinkering temperatures, and supplementary cementitious materials (SCMs) in replacement of cement, carbon capture and storage (CCS), and so on.

Rapid urbanization around the world has generated vast quantities of construction and demolition waste (CDW), which has in turn resulted in the dumping and landfilling of unprecedented volumes of CDW and the adverse social and environmental impacts of these practices (Wang et al., 2021; Xiao et al., 2012).

Considerable efforts have been made to shift the CDW streams from landfilling towards generating recycled concrete aggregates (RCA) (Soutsos et al., 2011; Xuan et al., 2016; Zhan et al., 2016a). During such recycling processes of CDW, waste hydrated cement paste (HCP) is separated from the RCA by heating and grinding to increase RCA performance (Poon et al., 2004), which method leaves 25% of fine concrete powder waste consisting mostly of HCP (Serpell and Lopez, 2013). The HCP waste is in turn reactivated as raw feed to produce recycled cementitious materials. In their experiment, Shui et al. (Shui et al., 2009) achieved 60% of the compressive strength of ordinary Portland cement paste for pastes incorporating HCP dehydrated at 800 °C. Elsewhere, Serpell and Zunino (Serpell and Zunino, 2017) investigated phase change and hydration reactivity of the reactivated cementitious materials (RCMs) obtained by thermal processing of the HCP with different clinkering temperatures, residence times, and cooling rates. A maximum compressive strength of 31.2 MPa was achieved for the RCM pastes. Serpell and Lopez (Serpell and Lopez, 2013) identified 9 material and process factors including W/C ratio and addition of SCM of the HCP wastes, grinding duration and dehydration temperature in the reactivation process, and alkaline activator and OPC content in production of RCM pastes etc., whereby the highest strength obtained was 32.8 MPa at 28 days. Zhang et al. (Zhang et al., 2018) introduced ground granulated blast-furnace slag (GGBS) into the blended binder system with a 600 °C dehydrated cement paste (DCP). The compressive strength of the 1:3 GGBS/DCP binder paste was 37.5 MPa, while the plain OPC paste showed a higher strength of 48.2 MPa. Compared to the paste samples mentioned above, compressive strengths of the mortar samples prepared with the RCMs were even lower (Carriço et al., 2020).

The lower binding properties of RCM were ascribed to their undesirable phase assemblage and the relatively porous microstructure (Bogas et al., 2020; Bogas et al., 2022). When clinkering the HCP, C–S–H was observed to start to decompose at 500 °C and transform into dicalcium silicate (β-C_2S) (Tantawy, 2017; Yim et al., 2019). Meanwhile, calcium oxide (CaO) was found to form from the decomposition of

calcium hydroxide ($Ca(OH)_2$) at around 470 °C (Stepkowska et al., 2004), and calcium carbonate ($CaCO_3$), between 700 and 800 °C (Akca and Özyurt, 2018; Yim et al., 2019). In further experiments on concrete mixtures with added supplementary cementitious materials (SCMs), the low calcium-to-silicon ratio (Ca/Si) of the hydration products led to the formation of non-hydraulic low-lime calcium silicate minerals such as calcio-olivine (γ-C_2S), rankinite (C_3S_2), wollastonite (CS), and Gehlenite following heat exposure (Ashraf et al., 2017; Hewlett and Liska, 2019; Wang et al., 2019).

Fortunately, although the hydration reactivity of low-lime calcium silicates proved insufficient, they did exhibit enhanced carbonation reactivity (Ashraf and Olek, 2016; Mu et al., 2018), with pure β-C_2S attaining the highest carbonation rate, followed by the C_3S, γ-C_2S, C_3S_2, and CS phases. Other studies established that carbonation of these minerals formed $CaCO_3$ and polymerized silica gel, as presented in Eq. (1) below (Bukowski and Berger, 1979; Jang and Lee, 2016), both of which comprise cementitious properties.

$$Ca_xSi_yO_{x+2y} + xH^+ + xHCO_3^- \rightarrow xCaCO_3 + ySiO_2\left(gel\right) + xH_2O \quad (1)$$

Carbonation mechanisms for recycled concrete fines (RCF) in aqueous solutions were investigated with the aim of reducing the environmental footprint of cement and concrete industries and developing value-added SCMs (Shen et al., 2022; Zajac et al., 2020). Phase assemblance evolution was discussed in detail, and it was confirmed that the carbonation of cement pastes is limited by the macroscopic diffusion of CO_2. Mehdizadeh et al. (Mehdizadeh et al., 2022) investigated the effect of CO_2 pre-treatment on waste hydrated cement paste powders containing fly ash (FA) and ground granulated blast furnace slag (GGBS). The carbonation products of carbonated FA cement paste are mainly calcite, whereas calcite and aragonite co-exist in carbonated BS cement paste. Overall, both carbonated waste powders can be used as a new SCM up to 30% without compromising the 28-day strength. The influence of high-temperature CO_2 on

the carbonation performance of RCF was investigated to simulate the flue gas containing waste heat (Wu et al., 2022). The carbonation efficiency is greatly enhanced by increasing the temperature up to 100 °C, and the calcite becomes larger and more stable at higher carbonation temperatures.

One promising emerging strategy arising from the above valuable research findings is the utilization of carbonation for hardening of calcium silicate binders (Ashraf and Olek, 2018a; Bukowski and Berger, 1979; Chang, J. et al., 2016). A low-calcium clinker containing C_3S_2-γ-C_2S-C_2AS was synthesized at a sintering temperature of 1320 °C. Calcite, aragonite, and polymerization silica gels produced a compressive strength above 60 MPa after carbonation (Lu et al., 2018). Carbonation curing has also been considered for precast concrete products and as a method for accelerating β-C_2S reactions (El-Hassan et al., 2013; Fang and Chang, 2017; Rostami et al., 2011). Moreover, CO_2-curing enhances chloride binding of cement pastes (Song et al., 2022a), while the addition of fly ash and slag lowers chloride ion penetration resistance at the late age (Song et al., 2022b). Accordingly, developing enhanced modalities to produce recycled cementitious materials (RCM) from low temperature sintering of HCP and apply carbonation curing for strength gain as well as for long-term carbon capture and storage, is a highly relevant and valuable strategy.

The objective of the present study was to explore an innovative approach that could reduce CO_2 emissions and excessive consumption of valuable resources by producing low-carbon emission cementitious materials by recycling waste hydrated cement paste. Carbonation curing was employed to improve cementing and CO_2 capture and storage (CCS) capability. The stoichiometric combinations of the precursor materials (HCP and silica fume) were selected as critical factors affecting the mineralogy and microstructure of the RCMs, and thus their reaction behavior. The precursors were mixed and exposed to a temperature of 800 °C and subsequently quenched in air to ambient temperature. The compressive strengths of eight group of mortar samples prepared with four RCMs and two curing regimes were

measured. The microstructure and phase assemblage of the RCM and carbonated mortar samples were characterized via X-ray diffraction (XRD), thermogravimetric analysis (TGA), scanning electron microscopy (SEM), energy dispersive X-ray (EDX), and mercury intrusion porosimetry (MIP) to reveal the mechanisms during clinkering and carbonation curing. The environmental impacts of the new process were evaluated through life cycle assessments (LCA) considering Global Warming Potential (GWP) and Cumulative Energy Demand (CED).

2. Materials and methodology

The sample preparation process conducted in this study is summarized in Fig. 1 below. The hardened cement paste was ground and mixed with four contents of silica fume to achieve different Ca/Si ratios from 1.06 to 3.93. After calcination at 800 °C for 1 hour, the conglomerate was milled again to a particle size below 75 µm. Thereafter, eight groups of mortar samples were prepared with the four RCMs and water cured or carbonation cured for hardening. The detailed specimen preparation processes are introduced in the following sub-sections.

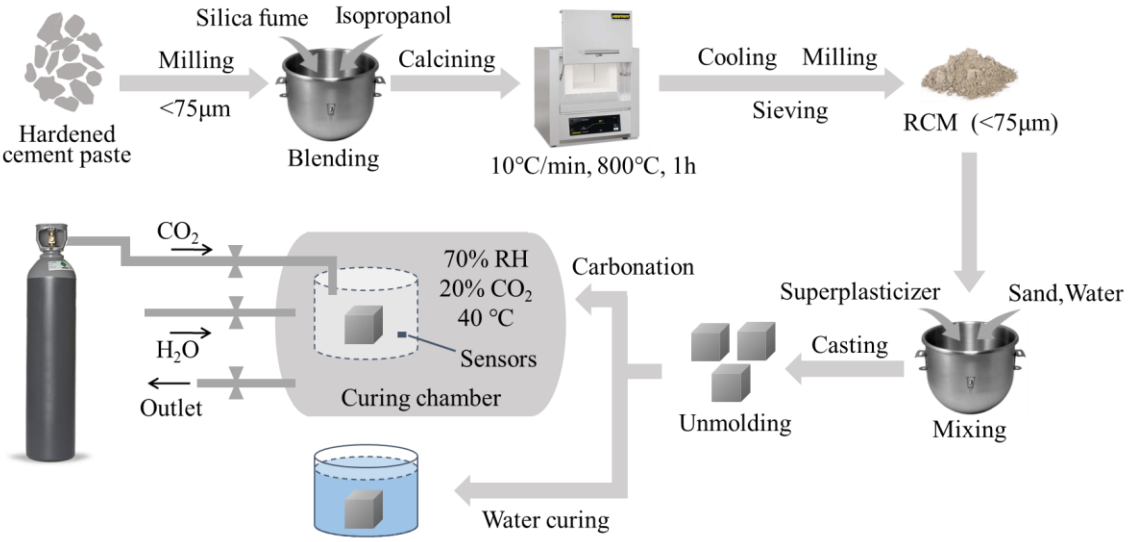

Fig. 1. Experimental mortar preparation procedure using RCM.

2.1. Materials and thermal activation of hardened cement paste

The chemical compositions of cement and silica fume were determined by X-Ray Fluorescence (XRF) analysis and are presented in Table 1 below. The cement (PO 42.5 R, Foshan Conch Cement Co. LTD) was mixed with tap water at a water-to-cement ratio of 0.3 for 3 minutes in a planetary mixer. The fresh paste was cast into 50 mm × 50 mm × 50 mm cubic molds and covered with a plastic membrane to prevent evaporation. After 1 day of hardening, the samples were demolded and cured in lime-saturated water for 56 days. The samples were then crushed into smaller than 1 cm^3 fragments and ground in a planetary ball grinder at 600 r/min until most of the powder could pass through a No. 200 mesh sieve (<75 μm).

The precursor admixture for clinkering was prepared by blending the cement paste powder with ratios of 0%, 10%, 20%, and 30% silica fume (LYGH-69587). The weighed powders were sufficiently homogenized in a jar mill, followed by blending with 20 wt.% isopropanol to facilitate optimal solid-state sintering during thermal activation. After exhaustive mixing for 10 min, the 4 mixtures were placed in alumina crucibles separately and sintered at 800 °C for 1 hour in a muffle furnace (Yamato FO811C).

This sintering temperature was much lower than the conventional practice for Portland cement, namely 800 °C against 1,450 °C for Portland cement. After heating, the clinkers were quenched in air. Once they had reached ambient temperature, the clinkers were ground using a ball mill at 350 r/min until the powders could pass through a No. 200 mesh sieve. Mild ball mill grinding was sufficient to crush the RCMs. The four RCMs were named as RCM-0, RCM-10, RCM-20, and RCM-30, respectively, with the numbers indicating the silica fume content.

Table 1. Chemical composition of cement and silica fume (%).

	CaO	SiO_2	Al_2O_3	Fe_2O_3	MgO	K_2O	SO_3	SrO
Cement	60.62	15.43	7.99	5.36	1.91	0.13	0.58	/
Silica fume	0.14	96.97	/	0.08	0.35	0.36	1.77	/

2.2. Preparation of the test samples and carbonation regimes

Four mortar mixtures denoted as M-0, M-10, M-20, and M-30 were prepared by using RCM-0/10/20/30, fine aggregate, water, and superplasticizer at a constant mass ratio, as shown in Table 2 below. The water-to-binder ratio was 0.4, and standard quartz sand with a maximum grain size of 1.18 mm was used as fine aggregate. A polycarboxylate-based superplasticizer (BASF RHEOPLUS® 410) was utilized to ensure the good workability of the fresh mixture.

Table 2. Mix proportions of the mortar samples (kg/m^3).

Mix Designs	RSM-0/10/20/30	Fine aggregate	Water	Superplasticizer
M-0/10/20/30	798.5	958.2	319.4	24.0

The mortar samples were prepared in a 10 L planetary mixer. The RCMs and fine aggregates were firstly dry-mixed for 3 minutes at low speed to ensure good dispersion. Then 80% of water was pre-mixed with superplasticizer and gradually added to the dry mix. After 3 minutes, the remaining water was added and mixed at high speed for a further 5 minutes. Lastly, the fresh mortar was cast into 50 mm × 50 mm × 50 mm cubic molds with vibration compaction for 50 seconds. The surface of the specimens was finished and covered with plastic film to avoid evaporation. After 24 hours' setting, the specimens were demolded. Two groups of specimens belong to each mixture were cured in lime-saturated water at 20 ± 3 °C or in a carbonation chamber for a further 27 days. Carbonation curing was performed in a controlled environment-chamber in which the carbon dioxide concentration was maintained at 20 ± 0.2%, the relative humidity was 70% ± 2%. The curing temperature was set at 40 °C to promote ion leaching and accelerate carbonation (Wang et al., 2017; Zhan et al., 2016b). After curing, the density of the RCM-0/10/20/30 samples were 2078, 2080, 2053, and 2039 kg/m^3, respectively. Compressive strength testing, MIP measurements, and SEM observation were conducted. In addition, parallel paste samples of the four mixtures without inclusion of fine aggregates were prepared for XRD and TG analysis to avoid any interference from quartz in the fine aggregates.

2.3. Characterization methods

Compressive strength testing of the mortar specimens was conducted via a SANS universal materials tester at a constant loading rate of 2.4 kN/s in accordance with ASTM C109/C109M-11 (Mater., 2011). Mean value and standard deviation were calculated from the results of three cubic specimens for each of the eight groups.

Phase assemblage of the RCMs and specimens after curing was studied using a Bruker D8 Advance X-ray diffractometer with Cu Kα radiation at 40 kV and 40 mA, over a 2θ ranging from 5 to 65° and a step length of 0.02° at a scanning rate of 2°/min. Small pieces cut from the center of the paste samples were dried by solvent exchange with isopropanol for 24 hours and in an oven at 40 °C for 24 hours to stop hydration and carbonation. About 5 g of the paste sample was ground into powder by mortar and pestle. The XRD patterns were analyzed using HighScore Plus software.

Thermogravimetric analysis (TGA) was conducted using a NETZSCH STA 449 F5 Jupiter thermal analyzer to further characterize the phase composition and content of calcium carbonates (including the high-crystalline, poor-crystalline and amorphous phases), utilizing the same batch of powder samples as for the XRD analysis. Mass loss of about 50 mg of the samples was recorded with a heating rate at 10 °C/min varying from 30 °C to 900 °C under a nitrogen atmosphere.

The microstructure of the mortar specimens was observed using a Phenom Prox G6 scanning electron microscope (SEM) equipped with an energy-dispersive X-ray (EDX) spectrometer. Hydration and carbonation of the mortar samples were stopped by immersing these latter in isopropanol and oven-drying them. For the morphology examination under the secondary electron (SE) mode, small pieces of fractured mortar samples were taken. For observation using backscattered electron (BSE), the samples were impregnated with epoxy and finely polished on variable grade emery paper and Buehler Texmet™ polishing cloth with 1 µm MetaDi™ polycrystalline diamond suspension. Following ultrasonic cleaning

in isopropanol, the samples were oven-dried once again. Prior to observation, the samples were coated with a gold film for 40 seconds to avoid any charging effect. EDX spectra were also acquired from selected points to obtain a quantitative identification of elemental composition.

Mercury intrusion porosimetry (MIP) tests were conducted with a Micromeritics Autopore IV 9500 porosimeter to characterize pore structure. Pore sizes ranged from 5° nm to 360° μm. The samples for MIP were taken from the mortar specimens and crushed into particles of approximately 5 mm × 5 mm × 5 mm. Isopropanol was used to eliminate any evaporable water.

2.4. Life cycle assessment (LCA)

The respective environmental impacts of producing Portland cement mortar versus the RCM mortar were calculated and compared through LCA in terms of GWP (IPCC 2021 GWP100) and CED. A GWP over a timeline of 100 years was applied, the CED values accounted for direct and indirect energy consumption, and the cradle-to-gate production of the RCM mortar was analyzed. The life cycle stages and system boundaries of the two mortar types are presented in Fig. 2 below. The selected functional unit in the present study was 1 ton. The Portland cement mortar had a water-to-cement ratio of 0.4 and a sand-to-cement ratio of 1.5. The life cycle inventory (LCI) data, including raw materials (i.e., silica fume, tap water, silica sand, Portland cement, superplasticizer, and CO_2), transportation, and the energy for milling, mixing, casting, compacting, and water curing were obtained from the Ecoinvent v3.8 database. The data were deemed reliable in respect of time because they were based on the well-established processes of cement and concrete manufacturing (Guignot et al., 2015; Viczek et al., 2020). The energy consumed to collect the HCP was excluded from the assessment as it was utilized at the time of CDW procurement, that is, outside the remit of this study. The milling and calcination of the HCP was likewise assumed to have been conducted at the recycling plant. According to references (Jain et al., 2020; Yazdani et al., 2021), the average distance from demolition site to recycling plant is about 10 to 20 km in China, Australia,

and India. Thus, a distance of 20 km was adopted for the present study. The life cycle inventory data for RCM calcination was determined based on records for metakaolin as the manufacturing process for both is similar (McLellan et al., 2011). The energy used for carbonation curing was based on the calculation from reference (Huang et al., 2019). The CO_2 absorption rate was obtained from thermogravimetric analysis. The LCA was conducted using Simapro V9.3 software in accordance with the recommendations of the International Organization for Standardization (ISO 14040, 2006).

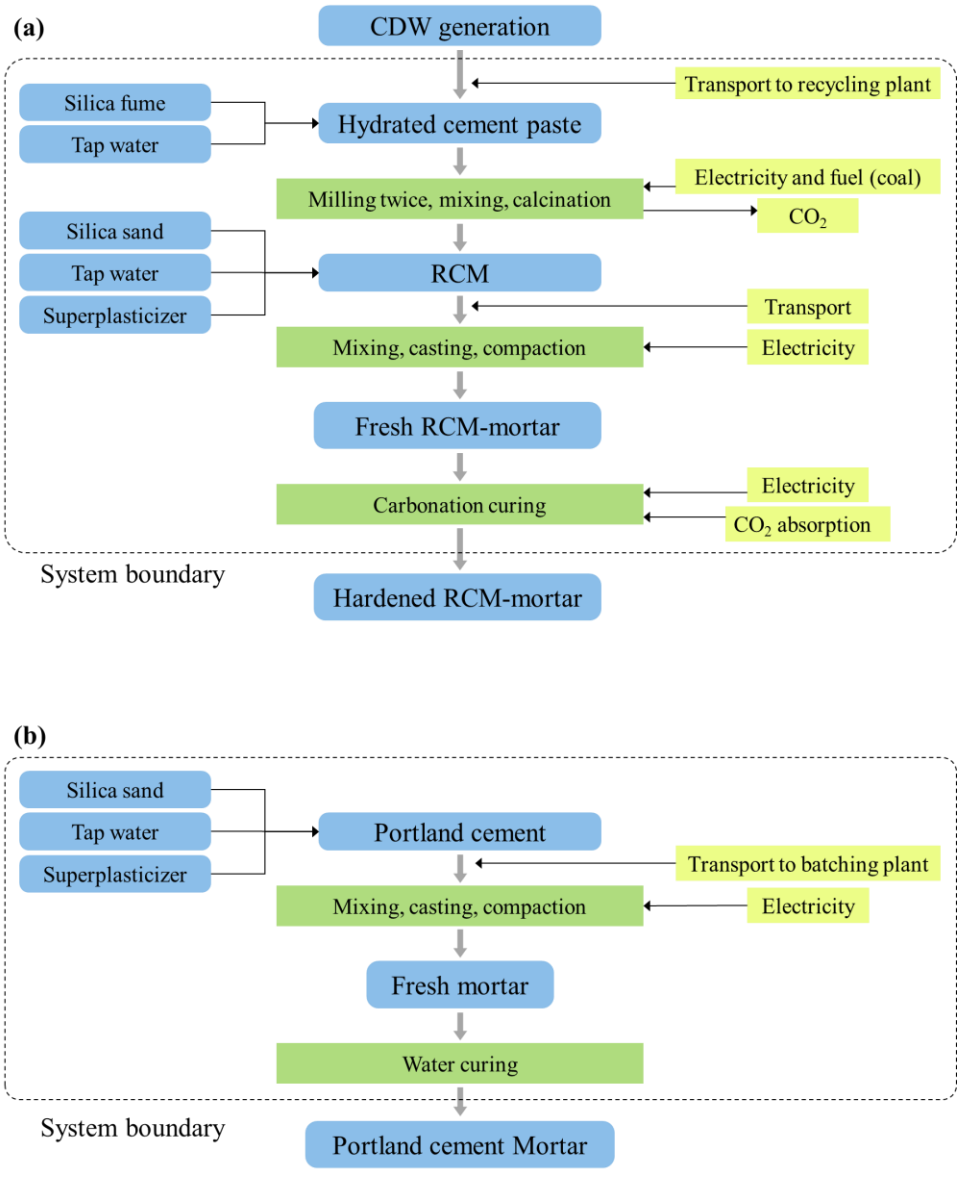

Fig. 2. Production processes and system boundaries for LCA of the RCM mortar and Portland cement mortar.

3. Results and discussion

3.1. Properties of the RCMs

Fig. 3 below illustrates the XRD patterns of the RCMs. In the RCM-0 sample, after thermal activation, noticeable solid-state reactions happen between the unhydrated cement and the hydration products. The C_3S and β-C_2S largely transformed to α'-C_2S and the portlandite and ettringite had completely decomposed to form CaO (Stepkowska et al., 2004). The disintegration of C-S-H produced β-C_2S and part of which transformed to α'-C_2S (Tantawy, 2017; Yim et al., 2019). For the RCM-10 sample, C_3S and β-C_2S also transformed to α'-C_2S. Moreover, the peak intensity of CaO was much lower in the RCM-10 than in the RCM-0 sample due to solid-state reactions occurring between the CaO and SiO_2. Two types of SiO_2 crystals were identified due to the transformation of amorphous silica fume to crystalline silica in a temperature range between 300 to 500 °C (Bettermann and Liebau, 1975). The RCM-20 and RCM-30 samples revealed a similar phase assemblage. With high silica fume replacement of 20% and 30%, the overall calcium-to-silicon ratio was found to have further decreased. Consequently, the peak intensities corresponding to C_3S and β-C_2S reduced significantly, and wollastonite (CS) was formed.

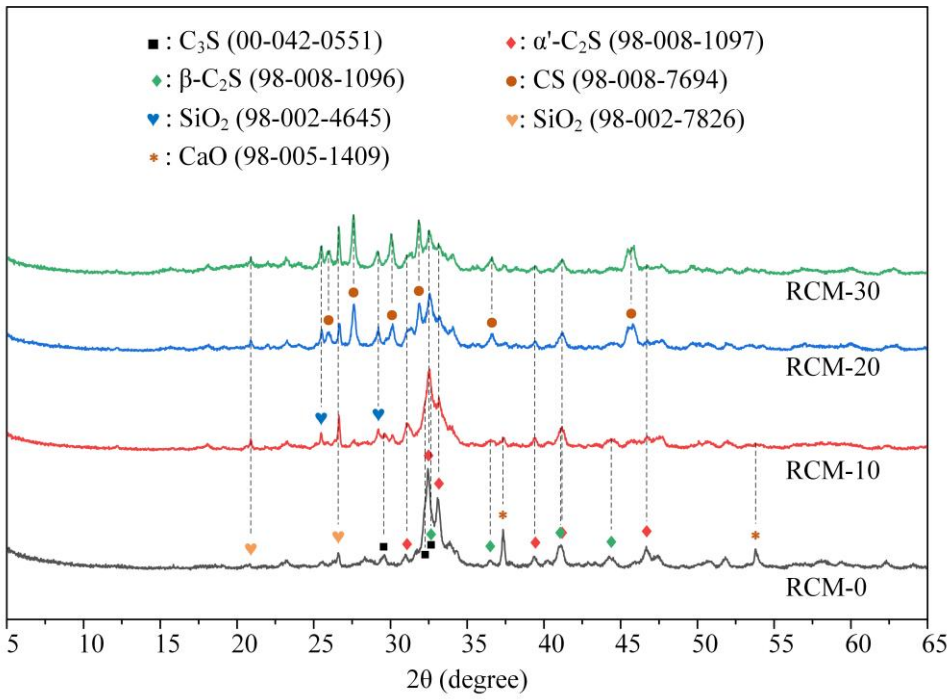

Fig. 3. XRD results of the RCMs.

3.2. Compressive strength

The compressive strengths of the RCM mortar samples are illustrated in Fig. 4 below. The letters 'W' and 'C' represent 'water' or 'carbonation' curing, respectively. For instance, 'M-10-C' means that the mortar used RCM-10 as binder with carbonation curing. As can be observed in Fig. 4, silica content in the RCMs significantly impacted on the compressive strength of the mortar samples. The respective compressive strengths of the M-0-W and the M-10-W specimens were 31.3 and 35.3 MPa. However, further increasing the silica fume content to 20% and 30% was found to jeopardize the compressive strength of the M-20-W and the M-30-W specimens to 7.1 and 2.6 MPa, respectively. The present authors ascribed this to the CS in the RCM-20 and RCM-30 having limited water reactivity.

After carbonation curing, a significant rise in compressive strength was recorded in all the mortar samples. The M-10-C achieved the highest compressive strength of 65.9 MPa, which represented 210.5% of its counterpart after water curing (M-10-W). Although the M-20-C and M-30-C samples showed lesser

compressive strengths of 40.9 MPa and 41.4 MPa, respectively, the effect of carbonation curing was still remarkable.

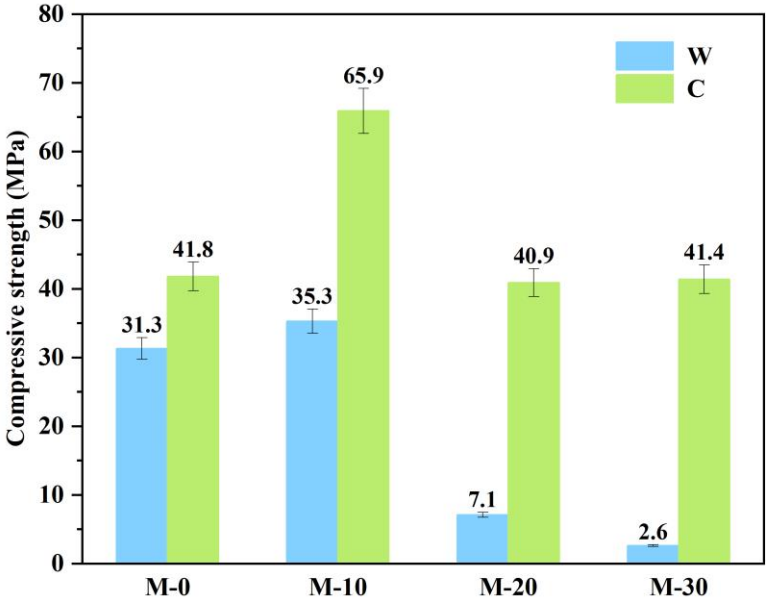

Fig. 4. Compressive strength of the mortar samples after water or carbonation curing.

3.3. Phase assemblage

As can be seen in Fig. 5a below, portlandite was the primary newly formed crystalline phase in sample M-0-W, whereas no diffraction peaks corresponding to CaO, C_3S, β-C_2S, and α'-C_2S were not observed after water curing of RCM-0. In the M-10-W sample, the hydration reaction consumed most of the C_3S, β-C_2S, and α'-C_2S phases in RCM-10. Less portlandite was observed in the M-10-W sample than that in the M-0-W sample, while higher amounts of ettringite and katoite (C_3AH_6) were formed. By comparing Fig. 5a with Fig. 3, it can be established that the hydration reaction in the M-20-W and M-30-W samples was relatively limited, while CS largely remained due to its low water reactivity.

As shown in Fig. 5b, carbonation curing strongly increased reactive intensity of the RCMs, especially the RCM-20 and RCM-30 with high CS content. During carbonation, the undersaturation of Ca^{2+} ions in the pore solution accelerated the dissolution rate of the RCMs and hence promoted the overall reaction

(Juilland et al., 2010; Nicoleau and Nonat, 2016). After carbonation curing, the reactive phases in the RCMs (CaO, C_3S, β-C_2S, α'-C_2S, and CS) were virtually complete, thus forming the $CaCO_3$ crystals calcite and vaterite. Amorphous phases combining poorly crystallized $CaCO_3$ and Ca-modified silica gel may also have formed from the decalcification of calcium silicates and C-S-H (Morandeau et al., 2014; Morandeau and White, 2015), but XRD technology was inadequate to identify these. Collectively, the above results established that these newly formed carbonation products did offer a sound cementitious capability and generated greater compressive strength than the hydration products. In the present authors' view, it is worth noting that the M-10-C sample had a distinctly higher vaterite content than the other three mixtures, which is in accordance with Lu et al.'s (Lu et al., 2022) finding that vaterite and aragonite have a positive effect on compressive strength development. Carbonation product content was quantified by TGA, and their impact on compressive strength is discussed in the following sections.

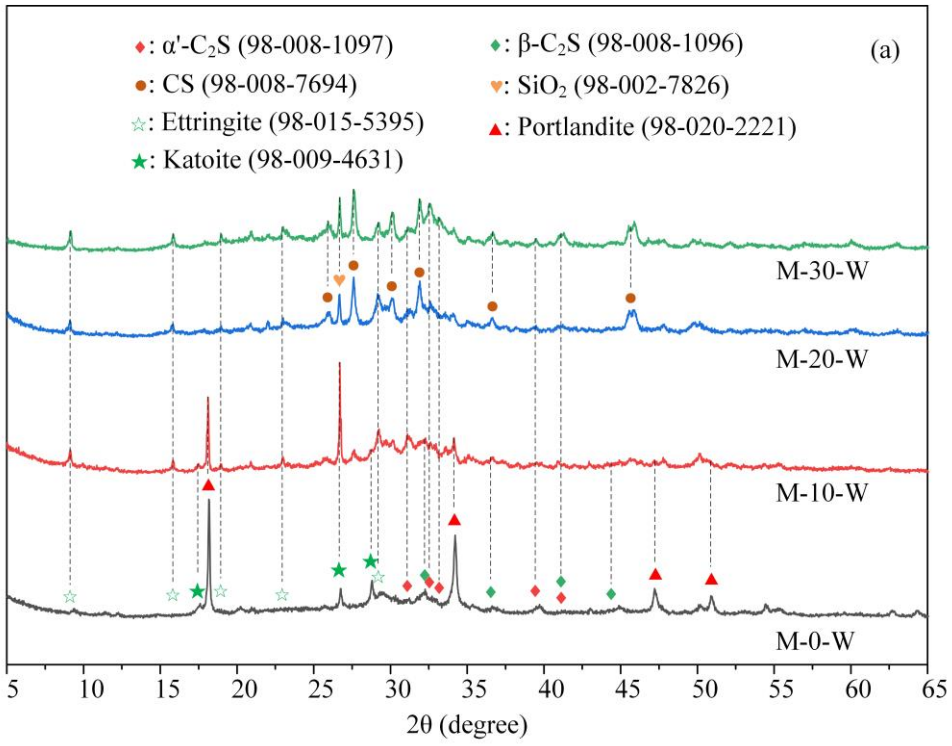

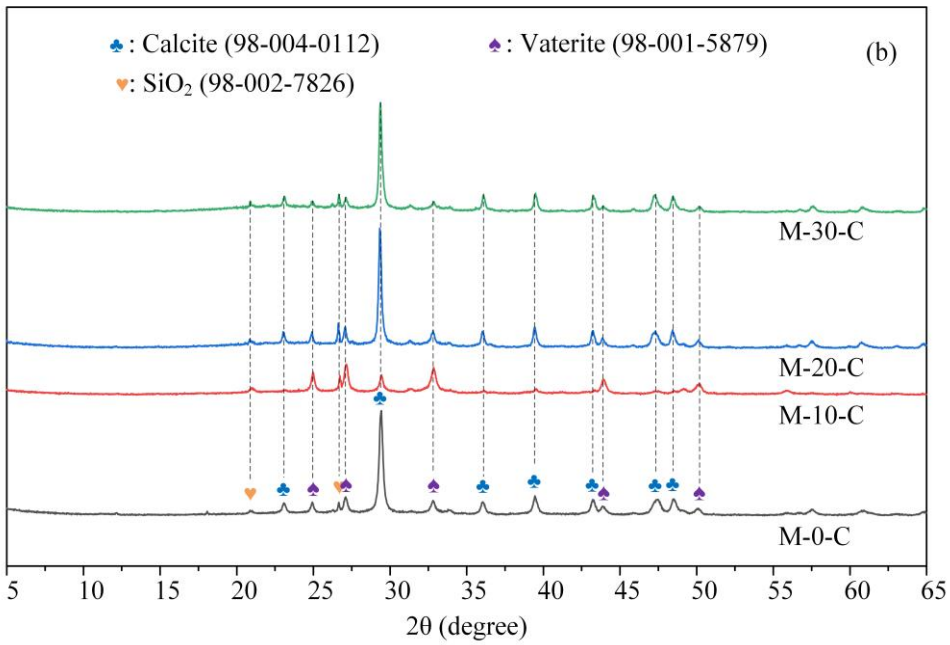

Fig. 5. XRD results of the paste samples after (a) water and (b) carbonation curing.

3.4. TGA results

The content of the hydration and carbonation products was analyzed by thermogravimetric (TG). The mass loss was divided into three sections (Zhan et al., 2021) as follows: (i) between 30 and 350 °C, the mass loss was primarily due to the release of evaporable water (Zhao et al., 2020) and the dehydration of ettringite (105–114 °C) (Krishnaiah and Singh, 2006), AFm (around 150 °C) (Zhi et al., 2022), C-S-H (from about 120 °C) (Singh and Garg, 1995), and katoite (around 200 °C) (Jiménez et al., 2022); (ii) the mass loss between 350 and 500 °C corresponded to the dehydration of portlandite in the water cured samples (Rostami et al., 2012); and (iii) in the carbonation cured samples, the mass loss in the wide temperature range between 400 and 800 °C was attributed to the decarbonation of $CaCO_3$ with different crystallinity, particle size, and polymorphism (Addadi et al., 2003; Ashraf and Olek, 2018b; Saillio et al., 2021).

As shown in Fig. 6a, a DTG peak ascribed to the decomposition of portlandite was obvious in the M-0-W sample. The corresponding peak was weaker in the M-10-W sample and could not be observed in the M-20-W and M-30-W samples. Due to the lower water reactivity of the RCMs with increased silica content, the overall mass loss was observed to have decreased correspondingly. The portlandite peak could barely be found in respect of the carbonation cured samples (Fig. 6b), while a mass loss caused by the decomposition of $CaCO_3$ from 400 °C indicated the co-existence of $CaCO_3$ with different crystallinity. According to Rostami et al. (Rostami et al., 2012), the thermal decomposition of good crystalline $CaCO_3$ occurs at temperatures above 720 °C (Short et al., 2001), while poorly-crystallized and metastable polymorphs (i.e., vaterite and aragonite) start to decompose at the lower temperature of 400 °C (Borges et al., 2010; Morandeau et al., 2014). However, the question as to whether amorphous and metastable $CaCO_3$ can be distinguished by temperature remains open to debate.

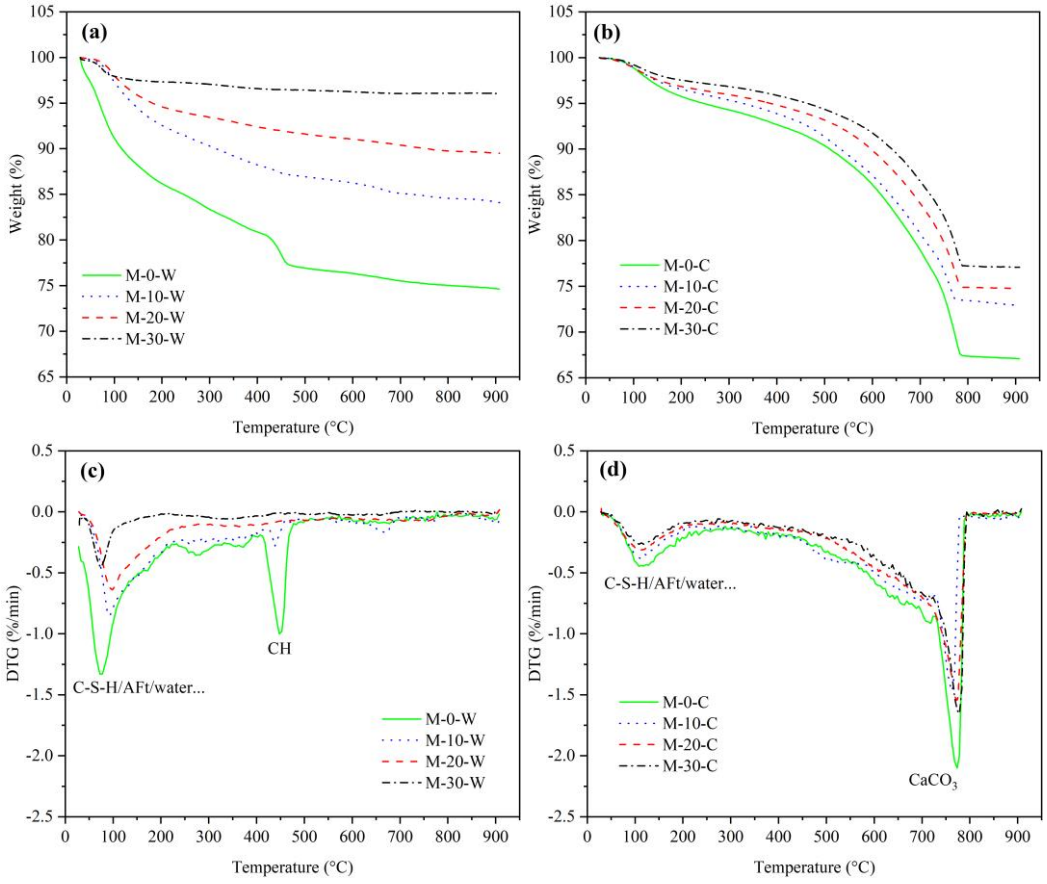

Fig. 6. TG and DTG curves of the mortar samples after (a, c) water and (b, d) carbonation curing.

In this study, the mass percentage of portlandite (CH) and $CaCO_3$ ($CC_{calcite}$ and $CC_{metastable}$) in the specimens was calculated through the following equations (Mehdizadeh et al., 2021b), the results of which are presented in Fig. 7 below:

$$\mathrm{CH}(\%) = w_{350-500} \times \frac{M_{\mathrm{CH}}}{M_{\mathrm{H_2O}}} \times 100\% \quad (2)$$

$$\mathrm{CC_{calcite}}(\%) = w_{720-800} \times \frac{M_{\mathrm{CaCO_3}}}{M_{\mathrm{CO_2}}} \times 100\% \quad (3)$$

$$\mathrm{CC_{metastable}}(\%) = w_{400-720} \times \frac{M_{\mathrm{CaCO_3}}}{M_{\mathrm{CO_2}}} \times 100\% \quad (4)$$

where $w_{350-500}$, $w_{720-800}$, and $w_{400-720}$ are the relative weight loss percentages between 350 and 500 °C, 720 and 800 °C, 400 and 720 °C, respectively; And M_{CH}, $M_{\mathrm{H_2O}}$, $M_{\mathrm{CaCO_3}}$, and $M_{\mathrm{CO_2}}$ are the molecular weight of portlandite, H_2O, $CaCO_3$, and CO_2, respectively.

It can be seen from Fig. 7a that the M-0-W sample contained the most hydration products and portlandite, and that either the mass loss below 350 °C or the amount of portlandite decreased with increased silica content in the RCMs. The extent of carbonation of the four mixtures also showed a decreasing trend with the increase in silica content in the RCMs. The M-0-C sample attained the highest overall $CaCO_3$ content of 57.4%, which corresponded to a 25.3% absorption capacity of CO_2.

In the carbonation cured samples, while the abundant $CaCO_3$ formed the skeleton of the matrix, the overall content of $CaCO_3$ did not prove to be proportional to the compressive strength. It is worth noting that the M-10-C sample with the highest compressive strength revealed the lowest percentage of calcite but the highest percentage of metastable $CaCO_3$. Previous studies have established that amorphous calcium

carbonate (ACC) is precipitated in the highly supersaturated pore solutions of Ca^{2+} and CO_3^{2-} ions (Brečević and Nielsen, 1989; Zhan et al., 2021). The ACC dehydrates and transforms to metastable vaterite, and finally the polymorphic transformation of vaterite to calcite takes place through dissolution and reprecipitation processes (Chang, R. et al., 2016; Rodriguez-Blanco et al., 2011; Wei et al., 2003). The formation of different polymorphs of $CaCO_3$ is reported to be dependent upon various factors such as concentration of CO_2 and Ca^{2+}, pH of the pore solution, temperature, relative humidity, phase assemblage before carbonation, and pore space for recrystallization of calcite (Liendo et al., 2022; Morandeau et al., 2014; Tai and Chen, 1995; Thiery et al., 2007). However, the exact conditions that favor the precipitation of these polymorphs are not well understood, and it is difficult to monitor the microenvironment inside the RCM mortar specimens (Mehdizadeh et al., 2021a; Shah et al., 2018).

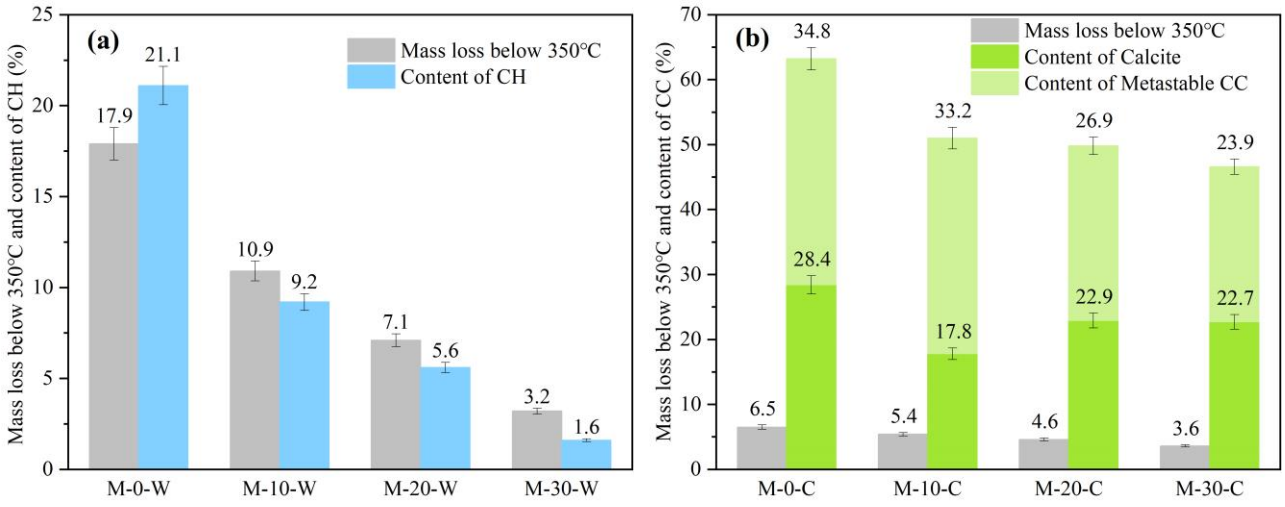

Fig. 7. Weight loss of (a) water cured and (b) carbonation cured mortar samples with content of CH and $CaCO_3$.

3.5. Microstructure observations

The microstructural changes of the mortar samples after water and carbonation curing were observed by SEM. As illustrated in Fig. 8 below, the smooth textured inclusions are sands, the sporadic bright regions are unreacted RCM particles, the light grey region represents hydration and carbonation products, and the

dark regions represent pores impregnated by epoxy. After water curing, the M-10-W sample comprised the densest matrix among the four water cured samples, which was consistent with its highest compressive strength. A darker interfacial transition zone (ITZ) surrounding the sands can be observed as circled by the dash lines (Fig. 8b), while in the M-0-W sample, pores can be observed surrounding the sands. Upon SEM analysis, the hydration products between the RCM particles seemed more porous than in the M-10-W sample, while the regions previously occupied by the RCM particles appeared compacted. With their higher silica content, a greater proportion of RCM particles was found to be unhydrated in the M-20-W and M-30-W samples. As a result, the matrix failed to fully develop into a dense and cohesive structure. The lack of hydration was consistent with the earlier result in this study that the compressive strength of these two samples was found to be marginal after water curing.

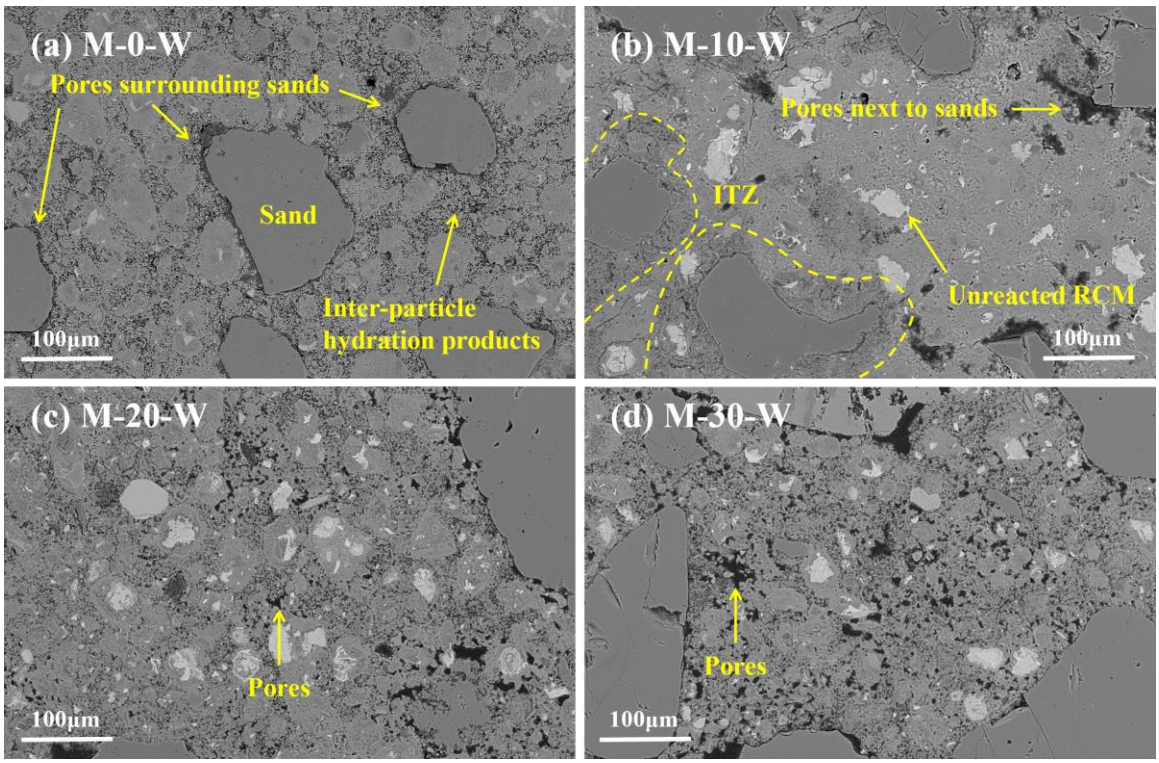

Fig. 8. The microstructure of the mortar specimens after water curing.

The samples after carbonation curing exhibited higher compacted microstructures than their counterparts after water curing due to the greater reaction of RCMs and filling effects of $CaCO_3$, as illustrated in Fig. 9 below. The refined microstructure accounted for their increased compressive strength. Moreover, the performance of the carbonated matrix is not only related to the phase composition and the amount of carbonates but also the morphological differences of the carbonate polymorphs and the binding capacity of the carbonate crystals (De Silva et al., 2006). As shown in Fig. 9b, the matrix of the M-10-C sample was well-defined and highly compacted. The enlarged inset exhibits vaterite crystals and agglomerated stacks of $CaCO_3$ crystals in various directions. The $CaCO_3$ crystals are restricted by the surrounding particles, indicating the creation of mechanical interlocking (Lu et al., 2022; Wang et al., 2020). This mechanical interlocking between $CaCO_3$ crystals is believed to create a strong microlevel force for carbonated products. Moreover, the $CaCO_3$ crystals can resist higher stress since they have greater strength than CH, C−S−H, and silica gel (Wang et al., 2020). Therefore, they contribute to the mechanical strength of carbonated products. In contrast, the M-0-C matrix was found to be looser (Fig. 9a). Dispersive cubic calcite grains were deposited between the sheets of Ca-modified silica gel, which explained why the M-0-C sample had generated more carbonates than the M-10-C sample, and yet had gained less compressive strength by the end of the experiment. Pores can be observed surrounding the sands in the matrix of the M-20/30-C samples. Those specimens can nevertheless still be seen to be much denser than the M-20/30-W after water curing.

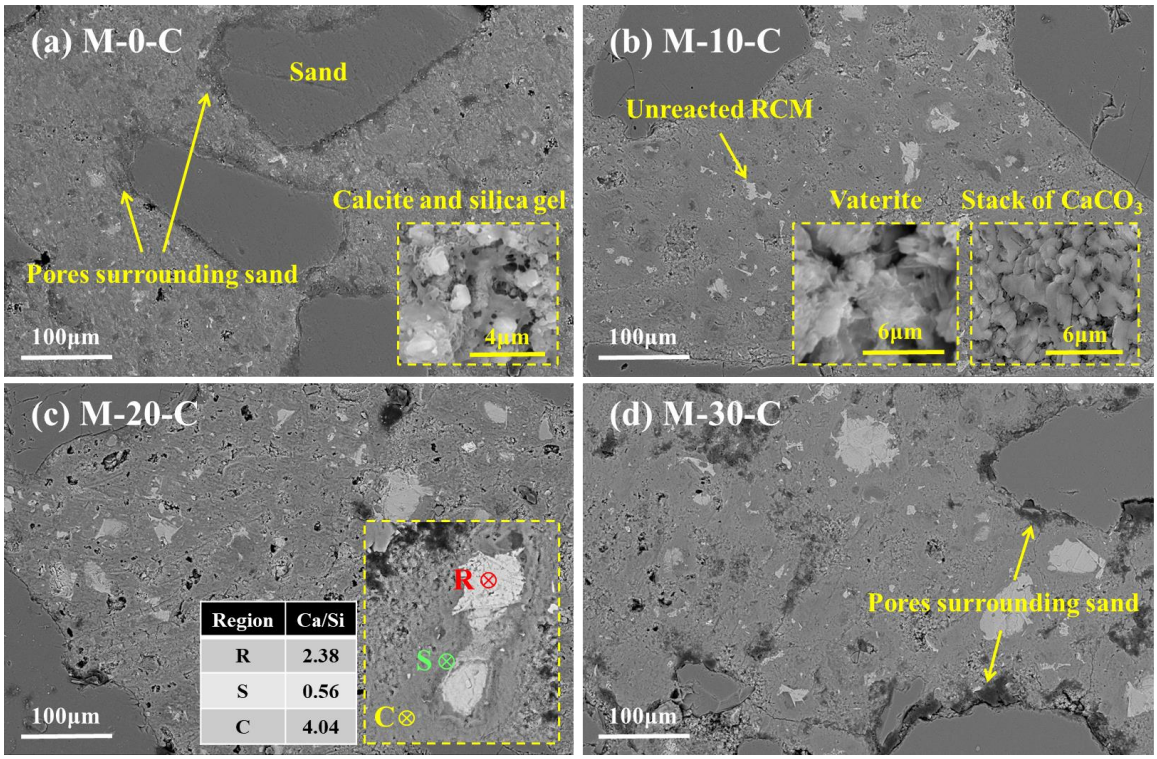

Fig. 9. Microstructure of the mortar specimens after carbonation curing.

Darker rims were found around the original RCM grains, which was believed to represent Ca-modified silica gel as reported from previous studies (Ashraf et al., 2017; Ashraf et al., 2016). As shown in Fig. 9c, the average atomic Ca/Si ratios around RCM particles were characterized by EDS analysis. Three zones based on the gray scale were noted, namely, the remaining RCM (R), the Ca-modified silica gel (S), and the carbonated products (C). The Ca/Si ratio of the remaining RCM was 2.38, which matched the stoichiometric ratio between C_3S and C_2S. At the periphery of the unreacted RCM grains was the Ca-modified silica gel (S), the Ca/Si ratio of which was as low as 0.56. Lastly, although the Ca/Si ratio of the carbonated products exceeded 4, it did not achieve as high $CaCO_3$ levels because the X-ray signal was an averaged value with a spot size of a few micrometers (Mu et al., 2019).

3.6. Porosity and pore size distribution

The porosity and pore size distribution of the samples were measured by MIP as shown in Fig. 10. Pore sizes were divided into the three ranges of coarse pores (> 1 μm), large capillaries (0.05–1 μm), and small capillaries (6 nm–0.05 μm) (Kang et al., 2019; Li et al., 2021). After water curing, the M-0-W sample showed a porosity of 16.67% and a peak pore size centered at 0.04 μm. The M-10-W sample attained the same peak pore size, but its porosity was 0.59% lower. Fig. 10c furthermore illustrates that this M-10-W sample comprised more small capillary pores but fewer large capillary pores, which explains its higher compressive strength. The porosity of the M-20-W sample increased to 20.34% and the M-30-W sample revealed the largest overall porosity of 33.08% with a peak pore size increased to around 0.2 μm, which explained its negligible compressive strength of 2.6 MPa.

The peak pore sizes of the M-0/10/20-C samples were slightly higher after carbonation than those after water curing (Fig. 10b). However, by comparing Fig. 10c with Fig. 10d, their small capillaries significantly reduced. This was attributed to the precipitation of $CaCO_3$ taking place preferentially in the smaller pores with better water condensation, and ultimately resulting in the densification of pores smaller than 0.05 μm. After carbonation curing, $CaCO_3$ polymorphs with different crystallinity were formed. According to the XRD and the TGA results, the M-10-C sample had fewer carbonation products but a distinctly higher content of amorphous $CaCO_3$ and vaterite than the other three mixtures. The lower density of vaterite (2.65 kg/m^3) and amorphous $CaCO_3$ compared to calcite (2.71 kg/m^3) (Christy, 2017) led to an increase in particle size and solid volume. This is expected to decrease the overall porosity and hence promote strength development. Moreover, the M-10-C sample exhibited agglomerated stacks of $CaCO_3$ crystals with strong mechanical bonds, but the M-0-C matrix was much looser, and unfilled pores surrounded the sand particles in the M-20/30-C samples. This explains why the M-10-C sample had the highest compressive strength.

From the SEM and MIP results, a porous skeleton was formed during the first day of hardening. During carbonation, precipitation of $CaCO_3$ due to the ingress of CO_2 consumed the Ca^{2+} ions in the pore solution and facilitated the dissolution of calcium ions (Ca^{2+}) from the RCM particles. As suggested by reference (Huijgen et al., 2006), the silica gel was formed as a result of the dissociation and migration of Ca^{2+}. The depositing of $CaCO_3$ progressively filled the porous skeleton and contributed significantly to the strength gain.

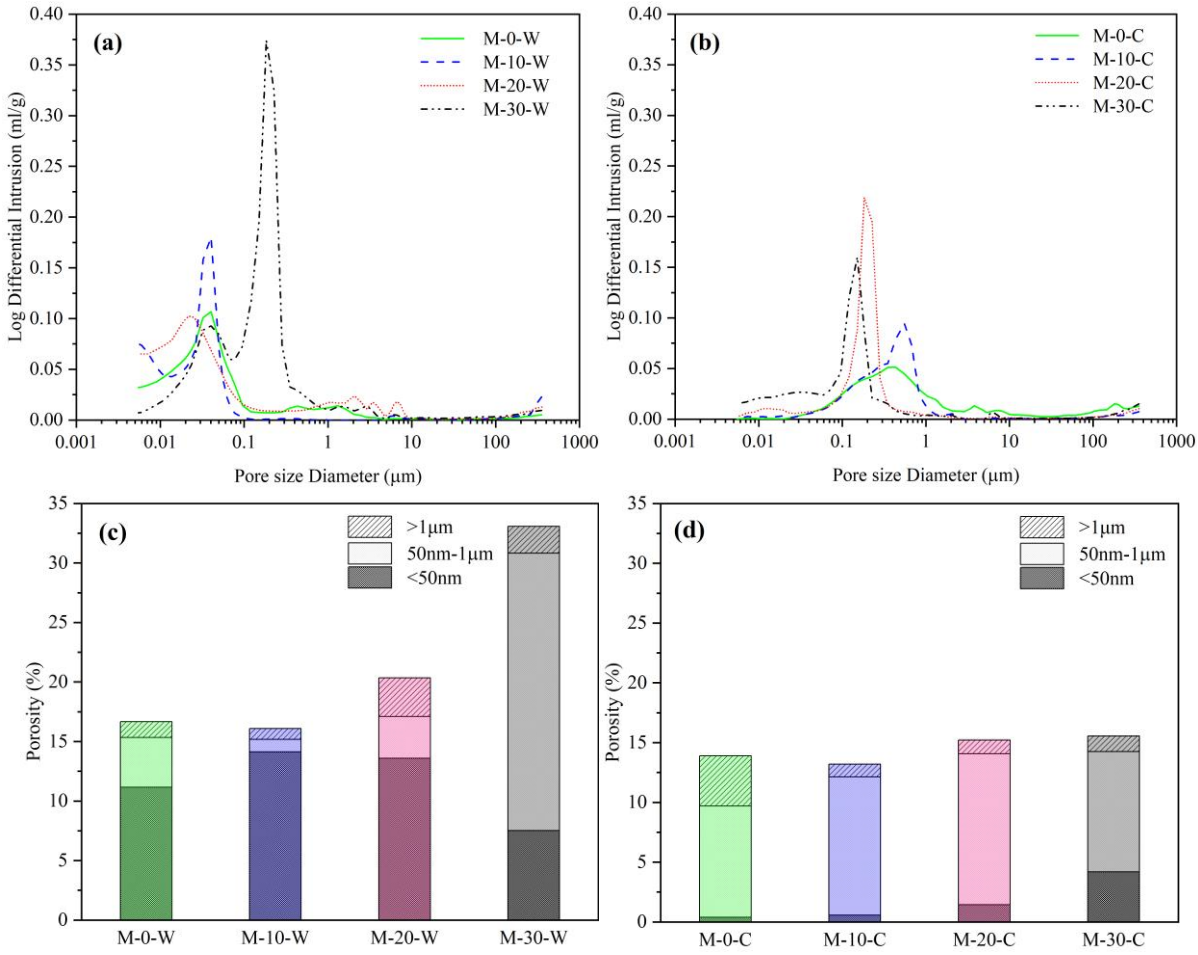

Fig. 10. Pore size distribution of the mortar samples after (a) water and (b) carbonation curing and (c) and (d) divided into three pore size ranges.

3.7. LCA results

Environmental impact of the Portland cement mortar and the RCM-mortar was evaluated by GWP and CED. The GWP of the Portland cement mortar was 378 kg CO_2 eq/kg, against only 93.6 kg CO_2 eq/kg in respect of the RCM-mortar, representing a 75.2% reduction. The GWP of RCM was 165 kg CO_2 eq/kg lower than that of Portland cement due to the saving in raw materials and the recycled calcium source. Another main reason for the lower GWP of the RCM mortar was that 152 kg CO_2 eq/kg was offset during the carbonation curing process.

In contrast to the beneficial effect in reducing CO_2 emissions, the overall CED required to prepare the RCM mortar proved 13.6% higher than that for the Portland cement mortar. This was mainly attributed to the additional amount of electricity usage during carbonation curing of the RCM mortar. In addition, the RCM and cement were found to share a similar CED even though the calcination temperature of the RCM was 600 °C lower. It should be noted that the energy consumption for the calcination and carbonation curing processes based on laboratory conditions may have been overestimated. Industrial-scale carbonation curing using cement kiln exhaust gas was reported by Liu et al. (Liu et al., 2022). CO_2 emission from cement factories and the cost of the carbonated bricks were both reduced. A 10,000-ton CO_2/y mineralization curing (CMC) process was demonstrated by Wang et al. (Wang et al., 2022). The GWP of CMC processes was similar to that of autoclaved curing, while CMC showed a significantly lower overall GWP after taking the differences in material formulation and CO_2 sequestration capacity into account.

These results demonstrated firstly, compared to the mortar mixture exclusively prepared with Portland cement, the utilization of RCM and carbonation curing confirmed a remarkable potential for CO_2 utilization and sequestration. Secondly, the use of natural raw materials could potentially be minimized

by recycling CDW, thus significantly reducing the reliance on land use to quarry raw materials and landfill to dispose of CDW waste.

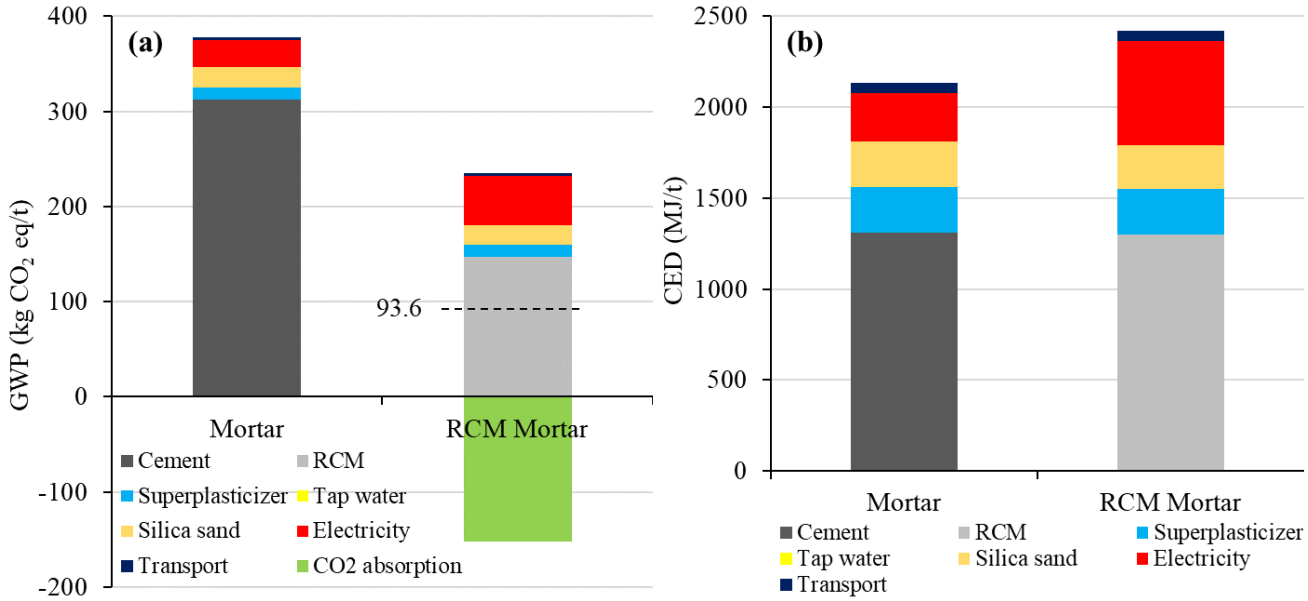

Fig. 11. Comparison of (a) GWP and (b) CED between RCM-mortar and Portland cement mortar.

4. Conclusion

In this study, a novel approach was proposed to produce low-carbon RCMs by calcinating HCP waste with adjusted silica content. Reactivity of the RCMs was promoted by carbonation curing. Multiple characterization methods were utilized to characterize the phase assemblage, microstructure, porosity, and elemental distribution of the RCM mortar samples after water and carbonation curing. The following conclusions can be drawn:

1. After thermal activation, the minerals in the RCM-0/10 consisted of C_3S, β-C_2S, α'-C_2S, CaO, and SiO_2 crystals. For the RCM-20/30, high calcium phases i.e., C_3S, β-C_2S, and CaO decreased and large amount of wollastonite (CS) was formed. Therefore, the RCM-20/30 showed much lower hydration and carbonation reactivity than the RCM-0/10.

2. Phase assemblage of the M-0/10-W samples was mainly C-S-H, calcium aluminate hydrates, and portlandite. With a relatively compacted binder matrix, their compressive strengths of 31.3 and 35.3 MPa, respectively, while the M-20/30-W samples showed negligible compressive strength due to the limited overall hydration.
3. A significant rise in compressive strength was recorded in all the carbonation cured samples due to the increased reaction of the RCMs. Poorly crystallized $CaCO_3$, metastable vaterite, calcite, and Ca-modified silica gel were the main carbonation products. The M-10-C attained the highest compressive strength of 65.9 MPa as a result of its densest microstructure and tightly packed $CaCO_3$ crystals, despite containing fewer carbonation products than the M-0-C sample. The compressive strengths of the M-20/30-C samples also increased from below 10 MPa to above 40 MPa.
4. The RCM-mortar achieved a 284.4 kg CO_2 eq/kg (75.2%) reduction in GWP compared to the Portland cement mortar, which was due to the economy in raw materials and the recycled calcium source. The CED for the two mortars was proved to be similar, but the present authors would anticipate a reduction in CED for the RCM-mortar in the context of large-scale industrial applications.

In conclusion, the findings of this study provide a valuable contribution to sustainable cementitious material production and construction waste management in the future. The new approach facilitates carbon capture and storage and guarantees enhanced compressive strength of the mortar samples. In consideration of the application in mass production, further studies are necessary to evaluate the consistency of the HCP supply in the real waste streams. The residual siliceous fines along with the HCP wastes may take part in reaction during reactivation affecting the Ca/Si ratio of the RCM or remain inert as fillers. Besides the selected technical process in the present study, doping with impurities during reactivation would further

increase reactivity of the RCMs. The reactivation process and the carbonation regime can be further optimized to tailor the type, morphology, and size of calcium carbonate polymorphs and thus to produce estimable mortar and concrete. At last, a novel internal carbonation curing method is highly expected to improve the performance of specimens by supplying additional CO_2 throughout the cross section.

Declaration of competing interest

The authors declare that they have no known competing financial interests or personal relationships that could have appeared to influence the work reported in this paper.

Acknowledgments

This work was supported by the National Science Fund for Distinguished Young Scholars [No. 52025081], the National Natural Science Foundation of China [No. 52008136], the Shenzhen Science and Technology Program [No. RCYX20200714114525013], and the Shenzhen Key Laboratory Launching Project [No. ZDSYS20200810113601005].

References

Addadi, L., Raz, S., Weiner, S., 2003. Taking advantage of disorder: amorphous calcium carbonate and its roles in biomineralization. Advanced Materials 15(12), 959-970.

Akca, A.H., Özyurt, N., 2018. Effects of re-curing on residual mechanical properties of concrete after high temperature exposure. Construction and Building Materials 159, 540-552.

Andrew, R.M., 2019. Global CO_2 emissions from cement production, 1928–2018. Earth System Science Data 11(4), 1675-1710.

Ashraf, W., Olek, J., 2016. Carbonation behavior of hydraulic and non-hydraulic calcium silicates: potential of utilizing low-lime calcium silicates in cement-based materials. Journal of Materials Science 51(13), 6173-6191.

Ashraf, W., Olek, J., 2018a. Carbonation activated binders from pure calcium silicates: Reaction kinetics and performance controlling factors. Cement and Concrete Composites 93, 85-98.

Ashraf, W., Olek, J., 2018b. Elucidating the accelerated carbonation products of calcium silicates using multi-technique approach. Journal of CO2 Utilization 23, 61-74.

Ashraf, W., Olek, J., Jain, J., 2017. Microscopic features of non-hydraulic calcium silicate cement paste and mortar. Cement and Concrete Research 100, 361-372.

Ashraf, W., Olek, J., Tian, N., 2016. Multiscale characterization of carbonated wollastonite paste and application of homogenization schemes to predict its effective elastic modulus. Cement and Concrete Composites 72, 284-298.
Barcelo, L., Kline, J., Walenta, G., Gartner, E., 2013. Cement and carbon emissions. Materials and Structures 47(6), 1055-1065.
Bettermann, P., Liebau, F., 1975. The transformation of amorphous silica to crystalline silica under hydrothermal conditions. Contributions to Mineralogy and Petrology 53(1), 25-36.
Bogas, J.A., Carriço, A., Tenza-Abril, A.J., 2020. Microstructure of thermoactivated recycled cement pastes. Cement and Concrete Research 138.
Bogas, J.A., Real, S., Carriço, A., Abrantes, J.C.C., Guedes, M., 2022. Hydration and phase development of recycled cement. Cement and Concrete Composites 127.
Borges, P.H., Costa, J.O., Milestone, N.B., Lynsdale, C.J., Streatfield, R.E., 2010. Carbonation of CH and C–S–H in composite cement pastes containing high amounts of BFS. Cement and concrete research 40(2), 284-292.
Brečević, L., Nielsen, A.E., 1989. Solubility of amorphous calcium carbonate. Journal of crystal growth 98(3), 504-510.
Bukowski, J., Berger, R.L., 1979. Reactivity and strength development of CO2 activated non-hydraulic calcium silicates. Cement and Concrete Research 9(1), 57-68.
Carriço, A., Bogas, J.A., Guedes, M., 2020. Thermoactivated cementitious materials – A review. Construction and Building Materials 250.
Chang, J., Fang, Y., Shang, X., 2016. The role of β-C2S and γ-C2S in carbon capture and strength development. Materials and Structures 49(10), 4417-4424.
Chang, R., Choi, D., Kim, M.H., Park, Y., 2016. Tuning Crystal Polymorphisms and Structural Investigation of Precipitated Calcium Carbonates for CO2 Mineralization. ACS Sustainable Chemistry & Engineering 5(2), 1659-1667.
Christy, A.G., 2017. A review of the structures of vaterite: the impossible, the possible, and the likely. Crystal growth & design 17(6), 3567-3578.
Churkina, G., Organschi, A., Reyer, C.P.O., Ruff, A., Vinke, K., Liu, Z., Reck, B.K., Graedel, T.E., Schellnhuber, H.J., 2020. Buildings as a global carbon sink. Nature Sustainability 3(4), 269-276.
De Silva, P., Bucea, L., Moorehead, D., Sirivivatnanon, V., 2006. Carbonate binders: Reaction kinetics, strength and microstructure. Cement and Concrete Composites 28(7), 613-620.
El-Hassan, H., Shao, Y., Ghouleh, Z., 2013. Effect of Initial Curing on Carbonation of Lightweight Concrete Masonry Units. ACI Materials Journal 110(4).
Fang, Y., Chang, J., 2017. Rapid hardening β-C2S mineral and microstructure changes activated by accelerated carbonation curing. Journal of Thermal Analysis and Calorimetry 129(2), 681-689.
Guignot, S., Touzé, S., Von der Weid, F., Ménard, Y., Villeneuve, J., 2015. Recycling Construction and Demolition Wastes as Building Materials: A Life Cycle Assessment. Journal of Industrial Ecology 19(6), 1030-1043.
Hewlett, P., Liska, M., 2019. Lea's chemistry of cement and concrete. Butterworth-Heinemann.
Huang, H., Wang, T., Kolosz, B., Andresen, J., Garcia, S., Fang, M., Maroto-Valer, M.M., 2019. Life-cycle assessment of emerging CO2 mineral carbonation-cured concrete blocks: Comparative analysis of CO2 reduction potential and optimization of environmental impacts. Journal of Cleaner Production 241.
Huijgen, W.J.J., Witkamp, G.-J., Comans, R.N.J., 2006. Mechanisms of aqueous wollastonite carbonation as a possible CO2 sequestration process. Chemical Engineering Science 61(13), 4242-4251.
Jain, S., Singhal, S., Pandey, S., 2020. Environmental life cycle assessment of construction and demolition waste recycling: A case of urban India. Resources, Conservation and Recycling 155, 104642.
Jang, J.G., Lee, H.K., 2016. Microstructural densification and CO2 uptake promoted by the carbonation curing of belite-rich Portland cement. Cement and Concrete Research 82, 50-57.
Jiménez, A., Rives, V., Vicente, M.A., 2022. Thermal study of the hydrocalumite–katoite–calcite system. Thermochimica Acta, 179242.
Juilland, P., Gallucci, E., Flatt, R., Scrivener, K., 2010. Dissolution theory applied to the induction period in alite hydration. Cement and Concrete Research 40(6), 831-844.

Kang, S.-H., Hong, S.-G., Moon, J., 2019. The use of rice husk ash as reactive filler in ultra-high performance concrete. Cement and Concrete Research 115, 389-400.
Krishnaiah, S., Singh, D., 2006. Determination of thermal properties of some supplementary cementing materials used in cement and concrete. Construction and Building Materials 20(3), 193-198.
Li, C.-z., Song, X.-b., Jiang, L., 2021. A time-dependent chloride diffusion model for predicting initial corrosion time of reinforced concrete with slag addition. Cement and Concrete Research 145, 106455.
Liendo, F., Arduino, M., Deorsola, F.A., Bensaid, S., 2022. Factors controlling and influencing polymorphism, morphology and size of calcium carbonate synthesized through the carbonation route: A review. Powder Technology 398.
Liu, J., Wang, Y., Li, Y., Tian, J., You, X., Mao, Y., Hu, X., Shi, C., 2022. Carbonated concrete brick capturing carbon dioxide from cement kiln exhaust gas. Case Studies in Construction Materials 17.
Lu, B., Drissi, S., Liu, J., Hu, X., Song, B., Shi, C., 2022. Effect of temperature on CO2 curing, compressive strength and microstructure of cement paste. Cement and Concrete Research 157.
Lu, B., Shi, C., Hou, G., 2018. Strength and microstructure of CO2 cured low-calcium clinker. Construction and Building Materials 188, 417-423.
Mater., A.S.T., 2011. ASTM C 109/C 109 M-11, Standard Test Method for Compressive Strength of Hydraulic Cement Mortars (Using 2-in. or 50-mm Cube Specimens).
McLellan, B.C., Williams, R.P., Lay, J., Van Riessen, A., Corder, G.D., 2011. Costs and carbon emissions for geopolymer pastes in comparison to ordinary portland cement. Journal of cleaner production 19(9-10), 1080-1090.
Mehdizadeh, H., Cheng, X., Mo, K.H., Ling, T.-C., 2022. Upcycling of waste hydrated cement paste containing high-volume supplementary cementitious materials via CO2 pre-treatment. Journal of Building Engineering 52.
Mehdizadeh, H., Ling, T.-C., Cheng, X., Mo, K.H., 2021a. Effect of particle size and CO2 treatment of waste cement powder on properties of cement paste. Can J Civil Eng 48(5), 522-531.
Mehdizadeh, H., Ling, T.-C., Cheng, X., Pan, S.-Y., Hung Mo, K., 2021b. CO2 Treatment of Hydrated Cement Powder: Characterization and Application Consideration. J Mater Civil Eng 33(4).
Morandeau, A., Thiéry, M., Dangla, P., 2014. Investigation of the carbonation mechanism of CH and C-S-H in terms of kinetics, microstructure changes and moisture properties. Cement and Concrete Research 56, 153-170.
Morandeau, A.E., White, C.E., 2015. In situ X-ray pair distribution function analysis of accelerated carbonation of a synthetic calcium–silicate–hydrate gel. Journal of Materials Chemistry A 3(16), 8597-8605.
Mu, Y., Liu, Z., Wang, F., 2019. Comparative Study on the Carbonation-Activated Calcium Silicates as Sustainable Binders: Reactivity, Mechanical Performance, and Microstructure. ACS Sustainable Chemistry & Engineering 7(7), 7058-7070.
Mu, Y., Liu, Z., Wang, F., Huang, X., 2018. Carbonation characteristics of γ-dicalcium silicate for low-carbon building material. Construction and Building Materials 177, 322-331.
Müller, D.B., Liu, G., Løvik, A.N., Modaresi, R., Pauliuk, S., Steinhoff, F.S., Brattebø, H., 2013. Carbon emissions of infrastructure development. Environmental science & technology 47(20), 11739-11746.
Nicoleau, L., Nonat, A., 2016. A new view on the kinetics of tricalcium silicate hydration. Cement and Concrete Research 86, 1-11.
Pade, C., Guimaraes, M., 2007. The CO2 uptake of concrete in a 100 year perspective. Cement and concrete research 37(9), 1348-1356.
Poon, C.S., Shui, Z.H., Lam, L., 2004. Effect of microstructure of ITZ on compressive strength of concrete prepared with recycled aggregates. Construction and Building Materials 18(6), 461-468.
Rodriguez-Blanco, J.D., Shaw, S., Benning, L.G., 2011. The kinetics and mechanisms of amorphous calcium carbonate (ACC) crystallization to calcite, via vaterite. Nanoscale 3(1), 265-271.
Rostami, V., Shao, Y., Boyd, A.J., 2011. Durability of concrete pipes subjected to combined steam and carbonation curing. Construction and Building Materials 25(8), 3345-3355.
Rostami, V., Shao, Y., Boyd, A.J., He, Z., 2012. Microstructure of cement paste subject to early carbonation curing. Cement and Concrete Research 42(1), 186-193.
Saillio, M., Baroghel-Bouny, V., Pradelle, S., Bertin, M., Vincent, J., de Lacaillerie, J.-B.d.E., 2021. Effect of supplementary cementitious materials on carbonation of cement pastes. Cement and concrete research 142, 106358.

Serpell, R., Lopez, M., 2013. Reactivated cementitious materials from hydrated cement paste wastes. Cement and Concrete Composites 39, 104-114.
Serpell, R., Zunino, F., 2017. Recycling of hydrated cement pastes by synthesis of α′H-C2S. Cement and Concrete Research 100, 398-412.
Shah, V., Scrivener, K., Bhattacharjee, B., Bishnoi, S., 2018. Changes in microstructure characteristics of cement paste on carbonation. Cement and Concrete Research 109, 184-197.
Shen, P., Zhang, Y., Jiang, Y., Zhan, B., Lu, J., Zhang, S., Xuan, D., Poon, C.S., 2022. Phase assemblance evolution during wet carbonation of recycled concrete fines. Cement and Concrete Research 154.
Short, N., Purnell, P., Page, C., 2001. Preliminary investigations into the supercritical carbonation of cement pastes. Journal of materials science 36(1), 35-41.
Shui, Z., Xuan, D., Chen, W., Yu, R., Zhang, R., 2009. Cementitious characteristics of hydrated cement paste subjected to various dehydration temperatures. Construction and Building Materials 23(1), 531-537.
Singh, M., Garg, M., 1995. Activation of gypsum anhydrite-slag mixtures. Cement and Concrete Research 25(2), 332-338.
Song, B., Hu, X., Liu, S., Shi, C., 2022a. Chloride binding of early CO2-cured Portland cement-fly ash-GGBS ternary pastes. Cement and Concrete Composites 134.
Song, B., Liu, S., Hu, X., Ouyang, K., Li, G., Shi, C., 2022b. Compressive strength, water and chloride transport properties of early CO2-cured Portland cement-fly ash-slag ternary mortars. Cement and Concrete Composites 134.
Soutsos, M.N., Tang, K., Millard, S.G., 2011. Concrete building blocks made with recycled demolition aggregate. Construction and Building Materials 25(2), 726-735.
Stepkowska, E., Blanes, J., Franco, F., Real, C., Pérez-Rodrıguez, J., 2004. Phase transformation on heating of an aged cement paste. Thermochimica acta 420(1), 79-87.
Summaries, M.C., 2021. Mineral commodity summaries. US Geological Survey: Reston, VA, USA 200.
Tai, C.Y., Chen, P.C., 1995. Nucleation, agglomeration and crystal morphology of calcium carbonate. AIChE Journal 41(1), 68-77.
Tantawy, M., 2017. Effect of high temperatures on the microstructure of cement paste. Journal of Materials Science and Chemical Engineering 5(11), 33.
Thiery, M., Villain, G., Dangla, P., Platret, G., 2007. Investigation of the carbonation front shape on cementitious materials: Effects of the chemical kinetics. Cement and Concrete Research 37(7), 1047-1058.
Viczek, S.A., Aldrian, A., Pomberger, R., Sarc, R., 2020. Determination of the material-recyclable share of SRF during co-processing in the cement industry. Resources, Conservation and Recycling 156.
Wang, B., Yan, L., Fu, Q., Kasal, B., 2021. A comprehensive review on recycled aggregate and recycled aggregate concrete. Resources, Conservation and Recycling 171, 105565.
Wang, D., Fang, Y., Zhang, Y., Chang, J., 2019. Changes in mineral composition, growth of calcite crystal, and promotion of physico-chemical properties induced by carbonation of β-C2S. Journal of CO2 Utilization 34, 149-162.
Wang, D., Xiong, C., Li, W., Chang, J., 2020. Growth of Calcium Carbonate Induced by Accelerated Carbonation of Tricalcium Silicate. ACS Sustainable Chemistry & Engineering 8(39), 14718-14731.
Wang, T., Huang, H., Hu, X., Fang, M., Luo, Z., Guo, R., 2017. Accelerated mineral carbonation curing of cement paste for CO 2 sequestration and enhanced properties of blended calcium silicate. Chemical Engineering Journal 323, 320-329.
Wang, T., Yi, Z., Song, J., Zhao, C., Guo, R., Gao, X., 2022. An industrial demonstration study on CO2 mineralization curing for concrete. iScience 25(5), 104261.
Wei, H., Shen, Q., Zhao, Y., Wang, D.-J., Xu, D.-F., 2003. Influence of polyvinylpyrrolidone on the precipitation of calcium carbonate and on the transformation of vaterite to calcite. Journal of Crystal Growth 250(3-4), 516-524.
Wu, Y., Mehdizadeh, H., Mo, K.H., Ling, T.-C., 2022. High-temperature CO2 for accelerating the carbonation of recycled concrete fines. Journal of Building Engineering 52.
Xiao, J., Li, W., Fan, Y., Huang, X., 2012. An overview of study on recycled aggregate concrete in China (1996–2011). Construction and building materials 31, 364-383.

Xuan, D., Zhan, B., Poon, C.S., 2016. Development of a new generation of eco-friendly concrete blocks by accelerated mineral carbonation. Journal of Cleaner Production 133, 1235-1241.
Yazdani, M., Kabirifar, K., Frimpong, B.E., Shariati, M., Mirmozaffari, M., Boskabadi, A., 2021. Improving construction and demolition waste collection service in an urban area using a simheuristic approach: A case study in Sydney, Australia. Journal of Cleaner Production 280, 124138.
Yim, H.J., Park, S.-J., Jun, Y., 2019. Physicochemical and mechanical changes of thermally damaged cement pastes and concrete for re-curing conditions. Cement and Concrete Research 125.
Zajac, M., Skibsted, J., Skocek, J., Durdzinski, P., Bullerjahn, F., Ben Haha, M., 2020. Phase assemblage and microstructure of cement paste subjected to enforced, wet carbonation. Cement and Concrete Research 130.
Zhan, B.J., Poon, C.S., Shi, C.J., 2016a. Materials characteristics affecting CO2 curing of concrete blocks containing recycled aggregates. Cement and Concrete Composites 67, 50-59.
Zhan, B.J., Xuan, D.X., Poon, C.S., Scrivener, K.L., 2021. Multi-scale investigation on mechanical behavior and microstructural alteration of C-S-H in carbonated Alite paste. Cement and Concrete Research 144.
Zhan, B.J., Xuan, D.X., Poon, C.S., Shi, C.J., 2016b. Effect of curing parameters on CO2 curing of concrete blocks containing recycled aggregates. Cement and Concrete Composites 71, 122-130.
Zhang, L., Ji, Y., Huang, G., Li, J., Hu, Y., 2018. Modification and enhancement of mechanical properties of dehydrated cement paste using ground granulated blast-furnace slag. Construction and Building Materials 164, 525-534.
Zhao, Z., Qu, X., Li, J., 2020. Microstructure and properties of fly ash/cement-based pastes activated with MgO and CaO under hydrothermal conditions. Cement and Concrete Composites 114, 103739.
Zhi, F., Jiang, Y., Guo, M.-Z., Jin, W., Yan, X., Zhu, P., Jiang, L., 2022. Effect of polyacrylamide on the carbonation behavior of cement paste. Cement and Concrete Research 156, 106756.